Nonlinear finite element analysis of reinforced concrete structures subjected to transient thermal loads

C. E. Zhou† and F. J. Vecchio‡

Department of Civil Engineering, University of Toronto, Toronto, ON M5S 1A4, Canada

(Received November 4, 2004, Accepted November 24, 2005)

Abstract. This paper describes a 2D nonlinear finite element analysis (NLFEA) platform that combines heat flow analysis with realistic analysis of cracked reinforced concrete structures. The behavior models included in the structural analysis are mainly based on the Modified Compression Field Theory and the Distributed Stress Field Model. The heat flow analysis takes into account time-varying thermal loads and temperature-dependent material properties. The capability of 2D nonlinear transient thermal analysis is then implemented into a nonlinear finite element analysis program VecTor2© for 2D reinforced concrete membranes. Analyses of four numerical examples are performed using VecTor2, and results obtained indicate that the suggested nonlinear finite element analysis procedure is capable of modeling the complete response of a concrete structure to thermal and mechanical loads.

Keywords: nonlinear finite element analysis; structural analysis; heat flow analysis; transient thermal loads; closed-form element stiffness.

1. Introduction

The need to incorporate fire loading into structural design has long been recognized, and is becoming a greater concern because of security-related issues. The investigation of the World Trade Centre disaster by the Building Performance Assessment Team, for example, indicated that the fire issues were crucial in the collapse of the twin towers. Reinforced concrete structures are also commonly exposed to thermal loads as the result of the design function of the structure, ambient conditions, heat of hydration, or exposure to fire. Therefore, there has been a growing interest in research on the advanced analysis and design of reinforced concrete structures subjected to thermal loads. Note that currently, transient thermal analyses are typically not employed in the design of reinforced concrete structures for thermal (fire) conditions. Rather, code provisions are typically based on detailing and cover requirements that, drawing on empirical data, provide an acceptable fire-rating in terms of the length of time that the structure must sustain its mechanical loads in the presence of fire without collapsing (e.g. three hours).

To understand the response of structures to thermal loads, one must isolate and consider various analysis stages. First, the thermal actions, which originate from increases in temperature and can be time varying, have to be differentiated from mechanical loads. Next, the temperature distribution has

† Corresponding Author, E-mail: mpezce@nus.edu.sg, Current Address: Centre for ACES, Department of Mechanical Engineering, NUS, 10 Kent Ridge Crescent, Singapore 119260, Singapore
‡ Professor

to be calculated according to these thermal actions. Here, one must consider the time effect in the transient heat analysis. Once the temperature distribution throughout the structure is known, one can evaluate the mechanical behaviour of the heated structure. Notably, some mechanical and thermal properties are highly temperature dependent, and some effects, like spalling and thermal creep, can be of significant importance in the analysis. Finally, one can predict the response by using the fire resistance factors or fire safety indices.

This paper attempts to implement the capability of 2D nonlinear transient thermal analysis into a nonlinear finite element analysis program for 2D reinforced concrete membranes. The time-varying thermal loads and temperature-dependent material properties are considered in this thermal analysis procedure. Taking advantage of realistic constitutive models, mainly based on the Modified Compression Field Theory (MCFT) (Vecchio and Collins 1986) and Distributed Stress Field Model (DSFM) (Vecchio 2000), one can obtain the complete response of all members within the structure, including external restraint forces, internal stresses, cracking development, and deflections.

The following discussion will provide descriptions on material properties' temperature dependency, thermal computational scheme, structural analysis procedure, case studies, and conclusions.

2. Temperature-dependent material properties

While concrete is generally a non-homogeneous, anisotropic medium composed of particles of aggregate held together by hydrated cement paste, it can be treated as a homogeneous isotropic material in heat analysis for simplicity. However, the temperature dependence of concrete's thermal properties has an important effect on heat transfer analysis. Moreover, the temperature-dependence of the mechanical properties will significantly affect the subsequent structural (stress and deformation) analysis.

2.1. Thermal-analysis-related properties

Temperature-dependent thermal properties (conductivity k and specific heat c) and physical properties (density ρ) make heat analysis nonlinear since the coefficient matrices in the final resultant equation are not constant but dependent on the temperature, which in turn is the unknown to be solved. The difficulties with the associated complexity in equation solution can be reasonably bypassed by assigning an average value of each property within every finite element at the current iteration step to simplify the formulations.

Since thermal properties at high temperature are quite difficult to obtain, only few data available in the literature (e.g. Shin, *et al.* 2002, Zhu and Chao 2002), their variation with temperature employed in this proposed implementation scheme are based on the Eurocode. They are briefly described as follows:

$$\rho(T) = \begin{cases} \rho(20^\circ\text{C}) & T \le 115\ ^\circ\text{C} \\ \rho(20^\circ\text{C})(1-0.02(T-115)/85) & 115\ ^\circ\text{C} < T \le 200\ ^\circ\text{C} \\ \rho(20^\circ\text{C})(0.98-0.03(T-200)/200) & 200\ ^\circ\text{C} < T \le 400\ ^\circ\text{C} \\ \rho(20^\circ\text{C})(0.95-0.07(T-400)/800) & 400\ ^\circ\text{C} < T \le 1200\ ^\circ\text{C} \end{cases} \quad (1)$$

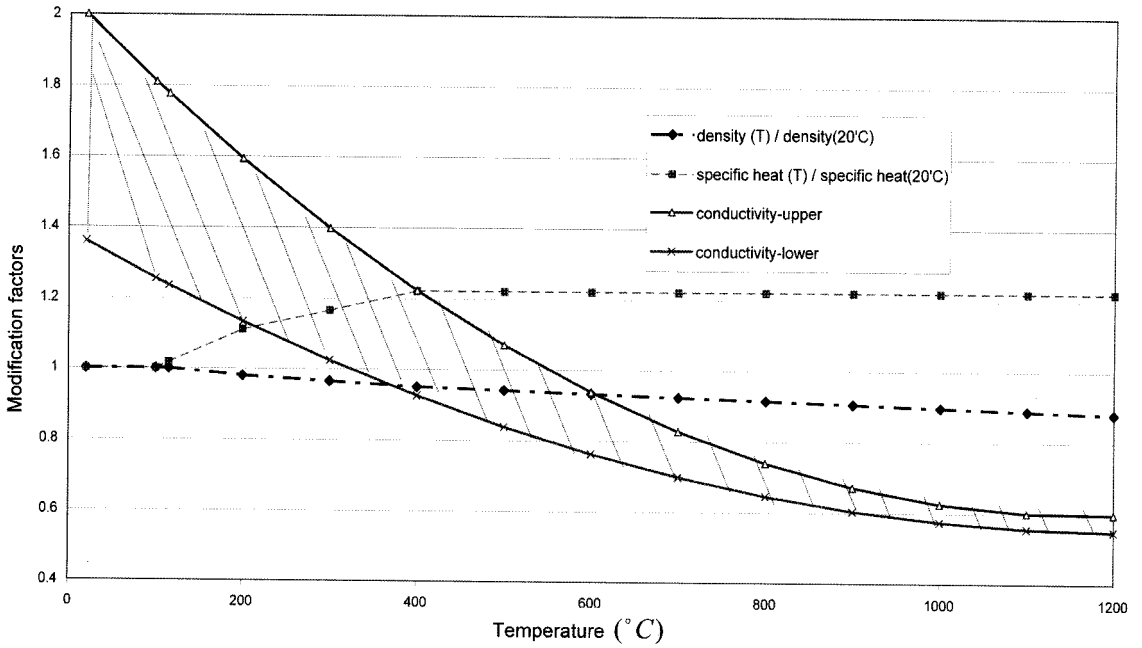

Fig. 1 Modification factors: thermal-analysis-related properties

where $\rho(T)$ is the density at temperature T(°C); and

$$c(T)=\begin{cases}900(J/kg\ K) & T\le 100\ ^{\circ}\mathrm{C}\\ 900+(T-100)\ (J/kg\ K) & 100\ ^{\circ}\mathrm{C}<T\le 200\ ^{\circ}\mathrm{C}\\ 1000+(T-200)/2\ (J/kg\ K) & 200\ ^{\circ}\mathrm{C}<T\le 400\ ^{\circ}\mathrm{C}\\ 1100(\ (J/kg\ K) & 400\ ^{\circ}\mathrm{C}<T\le 1200\ ^{\circ}\mathrm{C}\end{cases} \tag{2}$$

where $c(T)$ is the specific heat at temperature T(°C).

Regarding the conductivity k, the initial value at a reference temperature (20°C) can be used in the interpolation between the upper and lower limits given by Eurocode:

$$k^{upper} = 2.0 - 0.2451(T/100) + 0.0107(T/100)^2\ (W/mK) \tag{3}$$

$$k^{lower} = 1.36 - 0.136(T/100) + 0.0057(T/100)^2\ (W/mK) \tag{4}$$

With the reference at 20°C, modification factors for above properties are plotted in Fig. 1.

2.2. Structural-analysis-related properties

The material mechanical properties dominate in the subsequent structural analysis. However, both strength and stiffness deteriorate significantly under evaluated temperatures. In addition, continuity thermal stresses, induced in indeterminate structures due to thermal expansion, are heavily dependent on structural stiffness (Vecchio 1987).

Table 1 Some characteristic properties of concrete and steel at evaluated temperatures

Temperature (°C)	Concrete				Steel		
	Siliceous aggregates		Carbonate aggregates		f_y/f_y^{20}	f_u/f_u^{20}	E_s/E_s^{20}
	$f_c'/f_{c,20}'$	ε_c'	$f_c'/f_{c,20}'$	ε_c'			
20	1.00	0.0025	1.00	0.0025	1.0	1.0	1.0
100	1.00	0.0040	1.00	0.0040	1.0	1.0	1.0
200	0.95	0.0055	0.97	0.0055	1.0	0.81	0.90
300	0.85	0.0070	0.91	0.0070	1.0	0.61	0.80
400	0.75	0.0100	0.85	0.0100	1.0	0.42	0.70
500	0.60	0.0150	0.74	0.0150	0.78	0.36	0.60
600	0.45	0.0250	0.60	0.0250	0.47	0.18	0.21
700	0.30	0.0250	0.43	0.0250	0.23	0.07	0.13
800	0.15	0.0250	0.27	0.0250	0.11	0.05	0.09
900	0.08	0.0250	0.15	0.0250	0.06	0.04	0.07
1000	0.04	0.0250	0.06	0.0250	0.04	0.02	0.04
1100	0.01	0.0250	0.02	0.0250	0.02	0.01	0.02
1200	0.00	-	0.00	-	0.00	0.00	0.00

Note: ε_c' are net concrete strain values, with thermal strains excluded.

The mechanisms governing the chemical reactions and physical changes inside concrete and reinforcing steel, and how they affect the mechanical properties, are complex. Little experimental data is available (e.g. Castillo and Durrani 1990, Lie and Kodur 1996) and, surprisingly, they can differ significantly. Therefore, the values for normal-weight concrete and hot-rolled steel in Eurocode are employed. Some characteristics of concrete and reinforcing steel are shown in Table 1, where the property modification factors are directly given. If the tensile strength of concrete is to be taken into account, Eurocode calculates this reduction factor according to:

$$f(T)=\begin{cases}1.0 & T\le 100^{\circ}\mathrm{C}\\ 1.0-1.0(T-100)/500 & 100^{\circ}\mathrm{C}<T\le 600^{\circ}\mathrm{C}\\ 0.0 & 600^{\circ}\mathrm{C}<T\le 1200^{\circ}\mathrm{C}\end{cases} \tag{5}$$

As thermal elongation is believed to develop *progressively*, instead of giving explicit thermal expansion coefficients, the Eurocode provides thermal strains as follows.

- Concrete with siliceous aggregate:

$$\varepsilon(T)=\begin{cases}-1.8\times10^{-4}+9\times10^{-6}T+2.3\times10^{-11}T^{3} & T\le 700^{\circ}\mathrm{C}\\ 14\times10^{-3} & 700^{\circ}\mathrm{C}<T\le 1200^{\circ}\mathrm{C}\end{cases} \tag{6}$$

- Concrete with carbonate aggregate:

$$\varepsilon(T)=\begin{cases}-1.2\times10^{-4}+6\times10^{-6}T+1.4\times10^{-11}T^{3} & T\le 805^{\circ}\mathrm{C}\\ 12\times10^{-3} & 805^{\circ}\mathrm{C}<T\le 1200^{\circ}\mathrm{C}\end{cases} \tag{7}$$

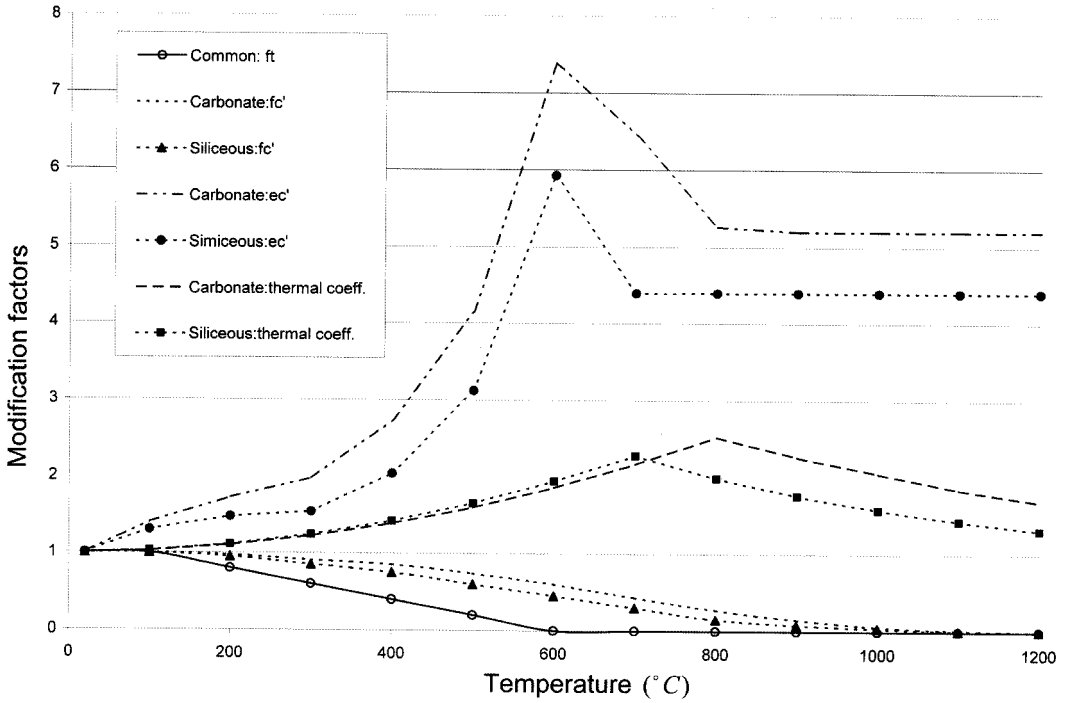

Fig. 2 Modification factors: concrete's structural-analysis-related properties

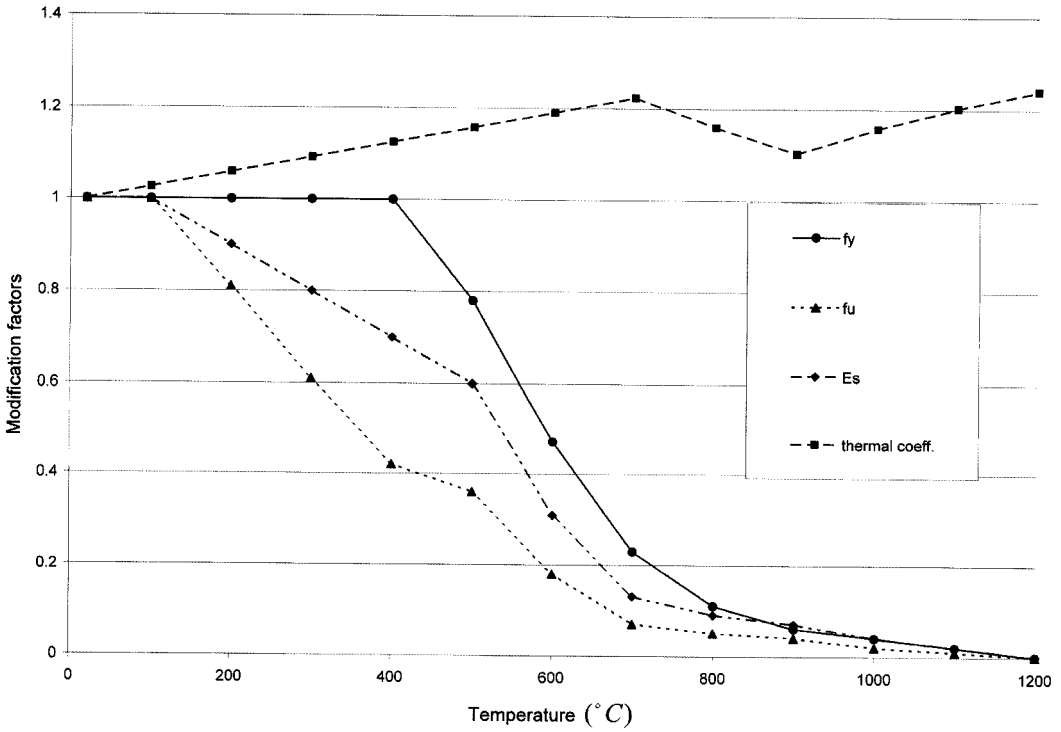

Fig. 3 Modification factors: steel's structural-analysis-related properties

• Reinforcing steel:

$$\varepsilon(T)=\begin{cases}-2.416\times10^{-4}+1.2\times10^{-5}T+0.4\times10^{-8}T^{3} & T\le750^{\circ}\mathrm{C}\\ 11\times10^{-3} & 700^{\circ}\mathrm{C}<T\le860^{\circ}\mathrm{C}\\ -6.2\times10^{-3}+2\times10^{-5}T & 860^{\circ}\mathrm{C}<T\le1200^{\circ}\mathrm{C}\end{cases} \tag{8}$$

Note that the above thermal strains are relative to the length at 20°C. Thus, with a reference at 20°C the modification (increasing in this case) factor for thermal expansion coefficient α can be calculated as:

$$f_{\alpha}(T)=\frac{\alpha(T)}{\alpha(20)}=\frac{\varepsilon(T)/\Delta T}{\varepsilon(20)_{,T}}=\frac{\varepsilon(T)/(T-20)}{\varepsilon(20)_{,T}} \tag{9}$$

Variation of these aforementioned modification factors (reduction or enhancement) are plotted in Fig. 2 and Fig. 3 for various concrete and steel, respectively.

3. Thermal computational scheme

Numerical techniques mainly used in the thermal analyses include Finite Difference Method and Finite Element Method, as detailed in the monograph by Ozisik (1994) and Zienkiewicz (2000), respectively. The current thermal computational scheme uses finite element spatial approximation and finite difference temporal discretization, as detailed hereunder.

The governing equation in terms of Cartesian coordinates for an isotropic material in a transient conduction problem is of the form:

$$\nabla\cdot(k\nabla T)+Q-\rho c\frac{\partial T}{\partial t}=0 \tag{10}$$

One can see that even under the assumption of *constant* thermal properties, the transient problems possess a *parabolic* nature with respect to its time dependence and an *elliptic* behavior with respect to the spatial coordinates.

The essential and natural boundary conditions are normally of the forms:

$$T=\bar{T}(x,y) \quad \text{on} \quad \Gamma_T \tag{11}$$

$$-k\frac{\partial T}{\partial n}=\bar{q}_n \quad \text{on} \quad \Gamma_q \tag{12}$$

where $\bar{T}$ and $\bar{q}$ are the prescribed values of temperature and heat flux on the corresponding boundaries Γ_T and Γ_q.

In a standard Galerkin procedure, one first discretizes the physical domain into elements. In VecTor2, linear triangular, standard rectangular, and the 4-node quadrilateral elements are employed. Within the element, shape function constructed then postulates a spatial form for the dependent variable T as follows:

$$T\approx T^{h}=\sum_{i}N_i a_i=\mathbf{Na} \tag{13}$$

where **a** is the nodal temperature vector. Since the transient problem involves the time variable, the

so-called *partial discretization* is adopted:

$$T(x,y,t) \approx T^h = \sum_i N_i(x,y)a_i(t) = \mathbf{Na} \tag{14}$$

Clearly, the derivatives of **a** with respect to time t will remain in the final approximation, and one can expect that the resultant equation system will be a set of ordinary differential equations with respect to the independent variable time t.

The Galerkin-weighted residual method readily leads to the so-called *weak form* statement as follows:

$$\int_\Omega \nabla^T v k \nabla T d\Omega + \rho c \int_\Omega v \frac{\partial T}{\partial t} d\Omega - \int_\Omega vQ d\Omega + \int_{\Gamma_q} v\bar{q} d\Gamma - \int_{\Gamma_T} vk \frac{\partial T}{\partial n} d\Gamma = 0 \tag{15}$$

where a lower order of continuity is required in the choice of the trial function T, at the price of a higher continuity for test function v.

If the choice of T is restricted as satisfying the essential boundary condition along Γ_T, the last term in the left-hand-side of Eq. (15) can be omitted. That is,

$$\int_\Omega \nabla^T v k \nabla T d\Omega + \rho c \int_\Omega v \frac{\partial T}{\partial t} d\Omega - \int_\Omega vQ d\Omega + \int_{\Gamma_q} v\bar{q} d\Gamma = 0 \tag{16}$$

One can now notice that the natural boundary condition along Γ_q is satisfied since no variable T appears in the integrals taken along the boundary Γ_q in Eq. (16). With the above Galerkin procedure, the initial and essential boundary conditions do not appear explicitly in the formulations. Thus, the spatial interpolation functions must be chosen so as to satisfy the essential boundary conditions, and a temporal stepping scheme must be started from the initial condition – initial state of the temperature field.

Substituting the shape functions into the integration and prescribing the test functions as trial function will lead Eq. (16) to:

$$\int_\Omega \nabla^T N_j k \nabla T d\Omega + \rho c \int_\Omega N_j \frac{\partial T}{\partial t} d\Omega - \int_\Omega N_j Q d\Omega + \int_{\Gamma_q} N_j \bar{q} d\Gamma = 0 \tag{17}$$

Eq. (17) can be rewritten in a matrix system of ordinary differential equations as follows:

$$\mathbf{Ka} + \mathbf{C}\frac{d\mathbf{a}}{dt} + \mathbf{f} = 0 \tag{18}$$

In heat analysis, **K** is the conductance matrix which is symmetric and diagonally dominant; **C** is the capacitance matrix; **f** is the forcing term due to internal heat resources (e.g. heat of hydration) and natural boundary conditions; and **a** is the nodal vector containing the nodal values of dependent variable T.

The entries of matrices can be evaluated by:

$$K_{ij} = K_{ji} = \int_\Omega \nabla^T N_j k \nabla N_i d\Omega = \int_\Omega \left(\frac{\partial N_j}{\partial x} k \frac{\partial N_i}{\partial x} + \frac{\partial N_j}{\partial y} k \frac{\partial N_i}{\partial y} \right) d\Omega \tag{19}$$

$$C_{ij} = C_{ji} = \int_\Omega N_i \rho c N_j d\Omega \tag{20}$$

$$f_j = -\int_\Omega N_j Q d\Omega + \int_{\Gamma_q} N_j \bar{q} d\Gamma \tag{21}$$

It is worthy noticing that in the current procedure, the element matrices in closed-form are derived for all employed element types. Contributions from each element are then sequentially added to the contents of the global system matrices. After removing the nodal equations corresponding to the boundary nodes with essential boundary conditions, the remaining equations are ready for solution.

Unlike a set of *algebraic* equations in steady-state problems, the system forms a set of first-order *differential* equations in time t for transient problems. Thus, the solutions have to proceed with increasing time until the results are obtained over a prescribed time level or until the steady state is attained. The most common time stepping procedure, a two-point finite difference in time, is as follows:

$$\frac{d\mathbf{a}}{d} = \frac{T_{n+1} - T_n}{\Delta t} \tag{22}$$

During each time step, regarding at what time level to evaluate the temperature in the calculation of coefficient terms in Eq. (18), the most popular scheme is to use the *trapezoidal rule* which uses a linear interpolation between steps n and n+1:

$$T_{n+r} = (1-r)T_n + rT_{n+1} \tag{23}$$

Substituting Eq. (22) and Eq. (23) into Eq. (18) leads to the so-called *generalized mid-point method* (Belytschko and Hughes 1983):

$$\mathbf{K}(T_{n+r},\ t_{n+r})T_{n+r} + \mathbf{C}(T_{n+r},\ t_{n+r})\frac{T_{n+1} - T_n}{\Delta t} + \mathbf{f}(T_{n+r},\ t_{n+r}) = 0 \tag{24}$$

where $t_{n+r} = t_n + r\Delta t$ with subscript n representing the nth time step.

Eq. (24) can be rearranged as follows:

$$\left[\frac{\mathbf{C}_{n+r}}{\Delta t} + r\mathbf{K}_{n+r}\right]T_{n+1} = \left[\frac{\mathbf{C}_{n+r}}{\Delta t} - (1-r)\mathbf{K}_{n+r}\right](T_n) - \mathbf{f}_{n+r} \tag{25}$$

where $\mathbf{C}_{n+r}$ refers to $\mathbf{C}(T_{n+r}\ t_{n+r})$; likewise with $\mathbf{K}_{n+r}$ and $\mathbf{f}_{n+r}$.

In Eq. (25), different methods can be identified by changing the value of r from 0 to 1.0. Both the choice of $r = 1/2$ (Crank-Nicholsn method) for accuracy considerations (Heinrich and Pepper 1999) and $r = 2/3$(Galerkin method) for stability purposes (Lewis, *et al.* 1996) are recommended, with the former being the default choice in VecTor2.

Due to the implicit nature, an iteration loop over each time step is required to maintain accuracy in the solution process. That is, the coefficient matrices' evaluation, assembly and solution have to be performed in an iterative manner within each time step, which makes nonlinear transient analyses computationally intensive. An example equation corresponding to iteration step i+1 at time level n+1 is given below.

$$\left[\frac{\mathbf{C}^i_{n+r}}{\Delta t} + r\mathbf{K}^i_{n+r}\right](T^{\,i+1}_{n+1}) = \left[\frac{\mathbf{C}^i_{n+r}}{\Delta t} - (1-r)\mathbf{K}^i_{n+r}\right](T_n) - \mathbf{f}^{\,i}_{n+r} \tag{26}$$

4. Structural analysis procedure

The structural analyses in program VecTor2 are based on the concept that nonlinear analyses of reinforced concrete membranes can be achieved by incorporating the nonlinear element formulations into an iterative linear elastic analysis procedure.

Representation of the structure is accomplished with smeared reinforced concrete elements (triangles or quadrilaterals) and discrete steel reinforcing truss bars. To reflect the nonlinear behavior, the material stiffness matrix is defined by using realistic constitutive relationships, mainly based on the MCFT and DSFM. In an iterative manner, the secant stiffness approach is then applied to form the element stiffness matrix, which enables analyses to consider various types of strain-offset effects. The above analysis platform, with details available in reference (Vecchio 1990), allows predicting the response of reinforced concrete elements subject to in-plane normal and shear stresses with the second-order accuracy.

Similarly as in the thermal analysis, the closed-form stiffness matrix (Zhou and Vecchio 2005) for the four-node quadrilateral element with a fully-populated material stiffness is again adopted in the structural analysis.

5. Case studies

The four numerical examples investigated carry different objectives. The purpose of Problem 1 is to verify the temperature profile throughout the depth of a cross section. Problem 2 is proposed to

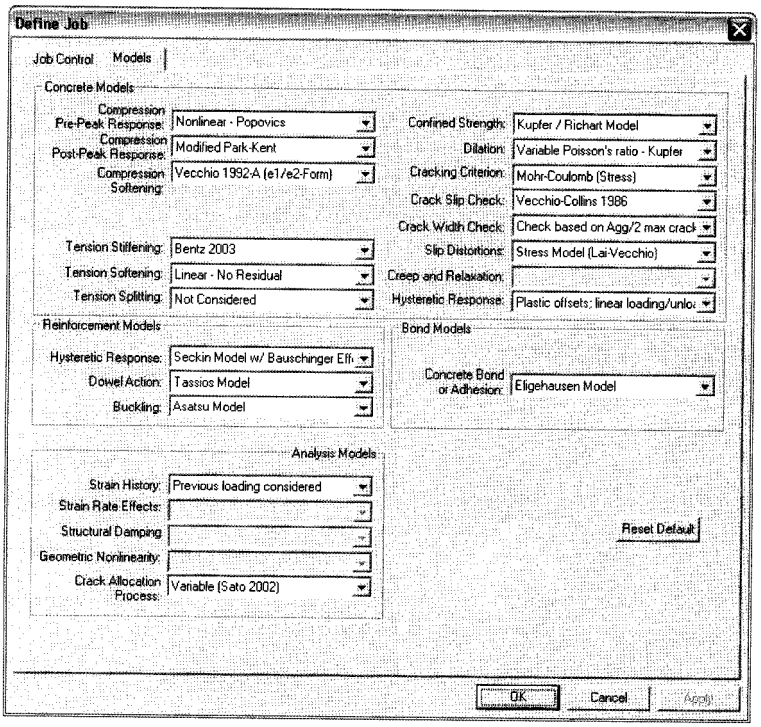

Fig. 4 Default material constitutive options in VecTor2

compare the accuracy of the results obtained from VecTor2 with those from ANSYS. Unlike Problems 1 and 2, Problem 3 requires a structural analysis be performed after the thermal analysis. The final problem is modeled after a specimen tested by Vecchio and Sato (1990) at the facilities of Ontario Hydro. Material constitutive laws, common to both Problem 3 and Problem 4, follow default options given by VecTor2 and are listed in Fig. 4.

5.1. Problem 1: Temperature profile

Consider the cross section of a long square bar (Fig. 5), initially at 0°C temperature everywhere. A constant temperature T=100°C is instantaneously imposed on the upper surface, while temperatures on the remaining surfaces are held at T=0°C. The purpose of this problem is to verify the temperature profile throughout the depth of a cross section. The model, a 11 × 11 uniform grid, is analyzed

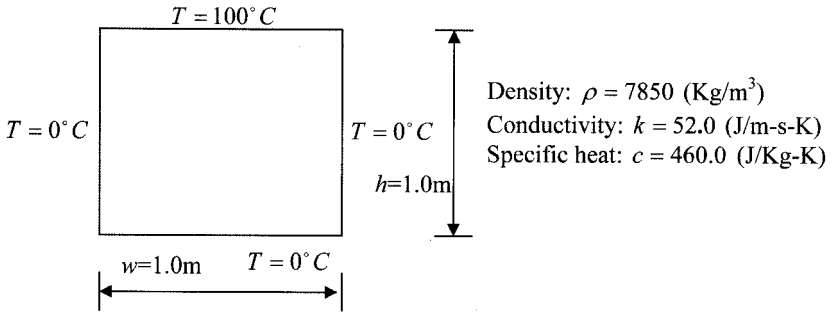

Fig. 5 Numerical Problem 1

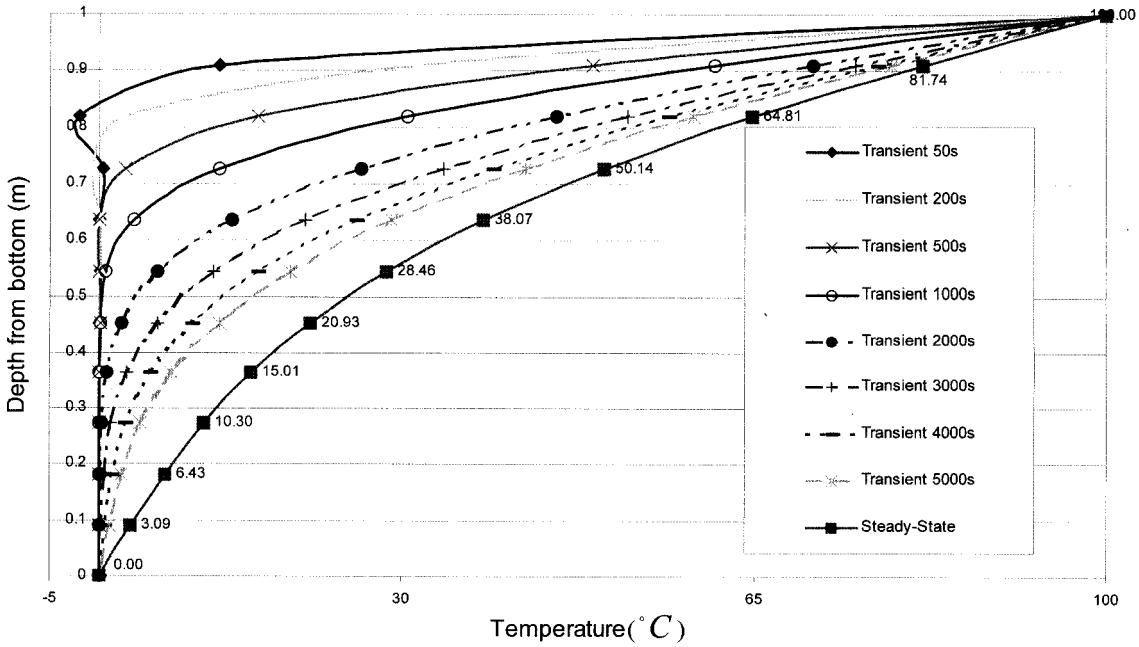

Fig. 6 Temperature profile through the depth of the cross section in Problem 1

through 100 time steps of 50s duration. The time stepping factor of 0.5 corresponds to the Crank-Nicholson scheme.

The temperature profiles for both steady-state and transient analyses are plotted in Fig. 6. It is observed that the transient thermal gradients are exceedingly nonlinear shortly after the thermal load is applied, while the steady-state analysis produces a fairly linear one. Also, the transient temperature profiles gradually approach the steady-state one as time advances. Thus, it can be expected that as time continues to proceed, there is one *ending* stage of transient thermal analyses when all transient effects have diminished and the corresponding temperature profile will be consistent with the one obtained from the steady-state analysis.

5.2. Problem 2: Accuracy comparison

This problem involves a simplified (phase change in the solidification process is ignored) casting process, detailed in the ANSYS Thermal Analysis Guide No. 858. The task is to track the temperature distribution in the steel casting and the L-shape sand mold as shown in Fig. 7.

A 2D analysis of a one unit thick slice is preformed. Due to symmetry, the lower half of the casting is modeled, with the finite element mesh given in Fig. 8. The conclusion time in this analysis is set at 3 hours, with the interval equal to 0.01 hour. The time stepping factor equals to 2/

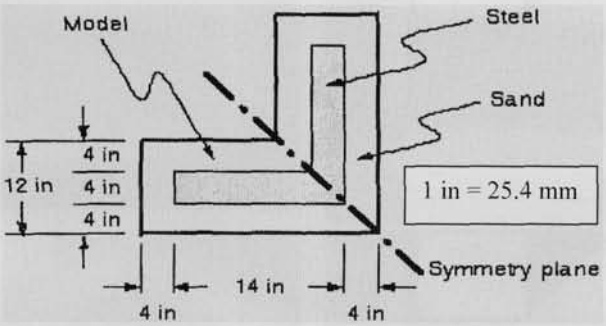

Fig. 7 Numerical Problem 2

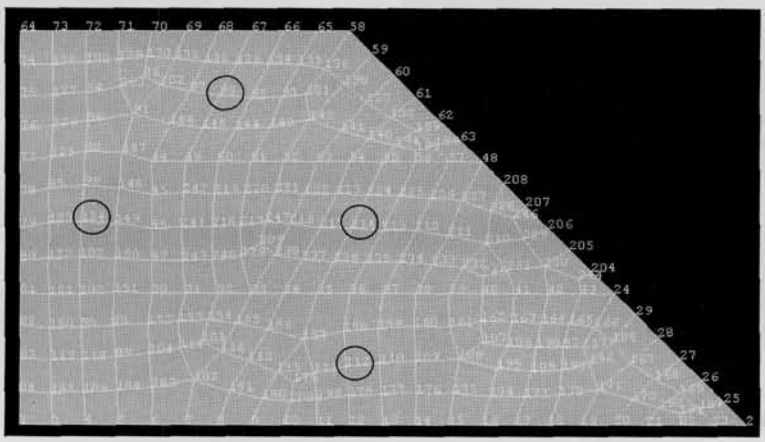

Fig. 8 The finite element model in Problem 2

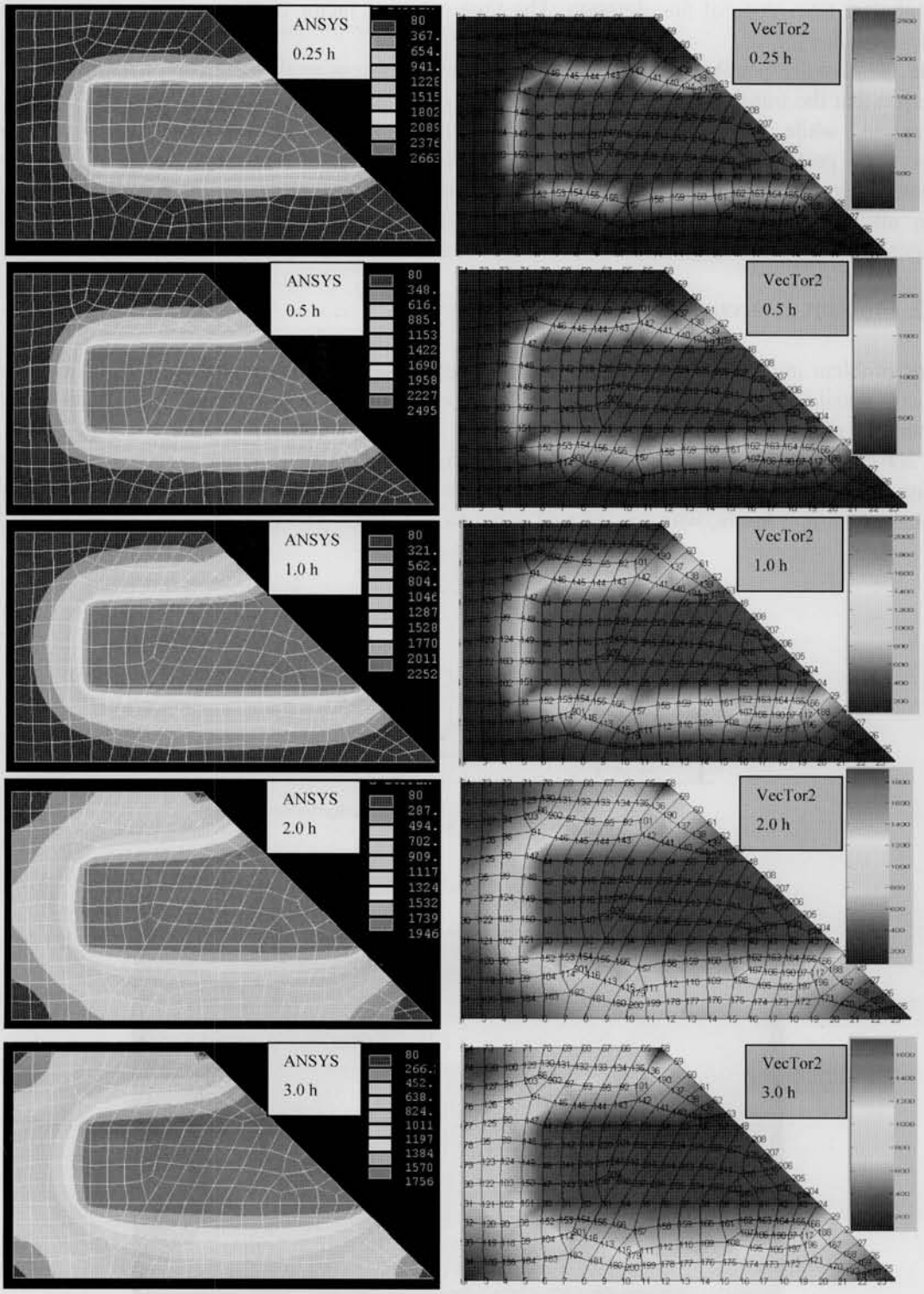

Fig. 9 Temperature contour plots in Problem 2

Table 2 Statistical comparisons in Problem 2

Rep. Node Number	T(VecTor2)/T(ANSYS)				
	0.25 h	0.5 h	1.0 h	2.0 h	3.0 h
214	2652.5/2512.2 =1.056	2469.6/2429.0 =1.017	2222.5/2189.7 =1.015	1924.8/1901.1 =1.012	1740.4/1721.7 =1.011
93	201.42/202.38 =0.995	388.92/456.30 =0.852	674.45/736.84 =0.915	954.07/985.18 =0.969	1086.7/1109.2 =0.980
124	187.52/178.31 =1.052	355.19/410.29 =0.866	613.98/669.21 =0.918	863.65/889.17 =0.971	979.65/995.42 =0.984
112	181.69/161.43 =1.125	349.68/396.52 =0.882	635.30/697.88 =0.910	966.71/1007.2 =0.960	1146.1/1176.3 =0.975
Mean	1.058	0.904	0.940	0.978	0.988
Mean of COV#(%)	(4.356+7.296+4.647+2.051+1.411)/5=3.95				

COV#: coefficient of the variation defined as percentage of ratio (standard deviation/mean).

3, corresponding to the Galerkin method.

For comparison purposes, the identical mesh system and time interval are used in both VecTor2 and ANSYS analyses. The results described below correspond to time steps at 0.25h, 0.5h, 1.0h, 2.0h and 3.0h. Contour plots of the temperature distribution for both analyses are shown in Fig. 9. Note that the temperature scale is lightly different in each plot. Also, the interpolation technique for contour plots in the ANSYS may not necessarily be bilinear, which is the case in the VecTor2's plots. Despite all that, one can readily see their similarity in capturing the heat conduction trend. In order to examine more precisely the difference between the two analyses, a statistical comparison of representative nodal (circled in Fig. 8) temperatures is given in Table 2. From both overall and specific comparisons, closeness in accuracy is observed.

5.3. Problem 3: Various thermal loads

Unlike Problems 1 and 2, this problem requires that a subsequent structural analysis be preformed after the heat analysis. The structure involved is a simply supported reinforced concrete beam as in Fig. 10, with material properties given in Table 3.

In this example, two reinforced concrete material types are used. One type models the plain concrete comprising the flange, while the other represents the web region of the beam with one

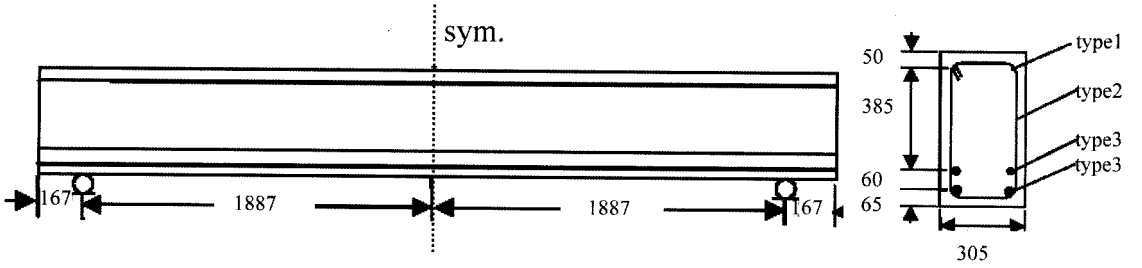

Fig. 10 Numerical Problem 3

Table 3 Material details in Problem 3

Material properties of concrete								
f_c' (MPa)	f_t' (MPa)		ε_c' ($\times 10^{-3}$)	E_c (MPa)			α_c ($\times 10^{-6}$/°C)	
24.1	1.88		2.00	24100			9.0	
Material properties of reinforcement								
Type	ϕ (mm)	A_s mm^2	f_y (MPa)	f_u (MPa)	E_s (MPa)	E_{sh} (MPa)	ε_{sh} ($\times 10^{-3}$)	α_s ($\times 10^{-6}$/°C)
1	13	253	345	700	200000	2000	5	11.5
2	7.5	$\rho = 0.099\%$	325	600	200000	2000	5	-
3	29	1282	555	900	200000	2000	5	11.5

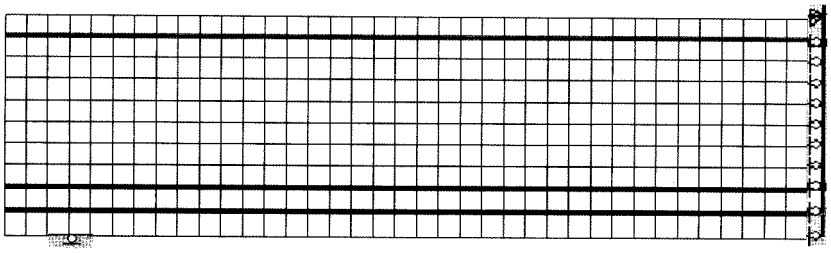

Fig. 11 The finite element model in Problem 3

smeared reinforcement component representing the stirrups. Also, two ductile steel reinforcement material types are utilized to model the longitudinal steel bars. The beam is subjected to gravity load in addition to thermal loads which simulate fire underneath. The analyses are expected to determine both the internal (e.g. stress) and external (e.g. deflection) responses of the beam at intermediate stages and at the conclusion of thermal loading.

As both the structural and loading conditions are symmetrical about the mid-span, only one half of the beam needs to be modeled, shown in Fig. 11. Nodes along the symmetrical line are restrained from displacements in the longitudinal direction, and the node at the support is restrained in the transverse direction. While the concrete is modeled by rectangular elements, truss bar elements are used for longitudinal reinforcing bars. The various thermal loads tested are plotted in Fig. 12. Note that the different load types provided are not intended to accurately simulate the fire in reality, but rather to illustrate some possible temperature loads.

Some typical results are discussed below, in terms of response of the structure.

• Reaction force at support:

Since the beam is statically determinate, no restraint force will result from thermal gradients, regardless of the fire load type. As a result, the reaction force at support remains constant at 8.25 kN, corresponding to the gravity load.

• Deflection at the beam's mid-span:

For the deflection at the steady-state condition, due to a linear thermal gradient, the curvature of the beam is constant along the length of the beam and equal to:

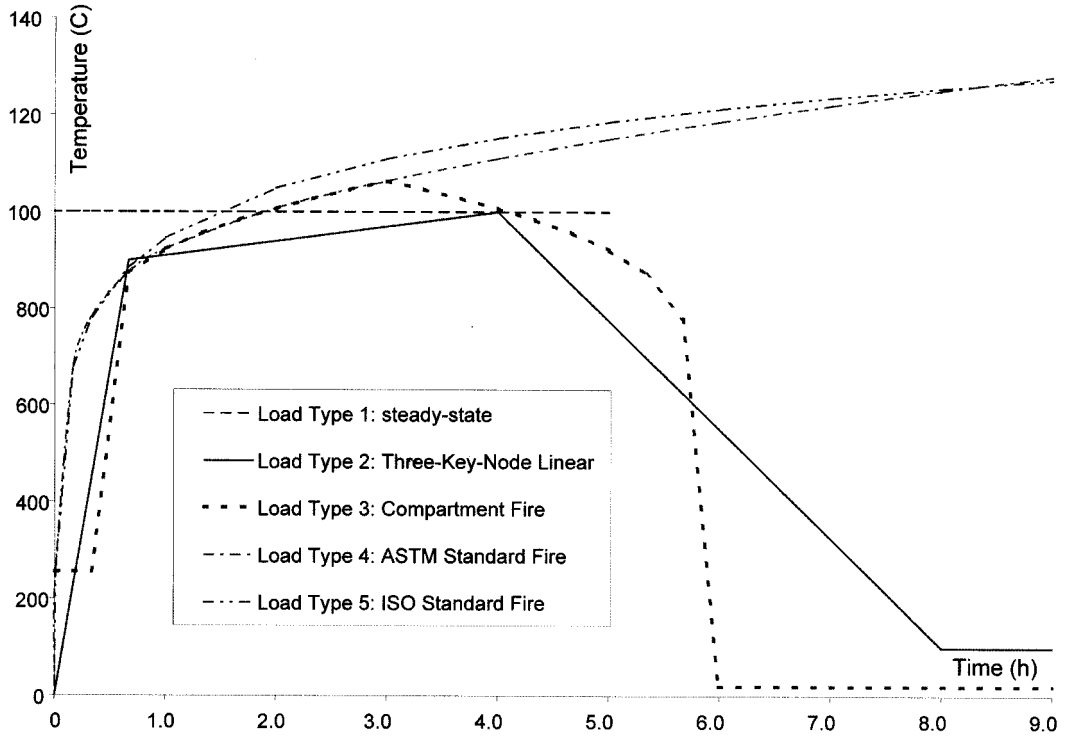

Fig. 12 Various thermal loads tested in Problem 3

$$\phi = \alpha_c \Delta T / h \tag{27}$$

where $\alpha_c = f \times \alpha_{c,20} = 2.035118 \times 9.0 \times 1.0^{-6}$ and thermal gradient is equal to 1000°C.

One can then use the first moment area theorem to calculate the deflection from the curvature as follows:

$$\Delta_{\min}^{T} = \phi \times \frac{L}{2} \times \frac{L}{4} = \frac{\alpha_c \Delta T L^2}{8h} = \frac{9 \times 10^{-6} \times 2.035118 \times 1000 \times (205.3 \times 2)^2}{8 \times 650} = 69.0 \text{ mm} \tag{28}$$

The deflection caused by the gravity load can be calculated as:

$$\Delta_{\text{mid}}^{G} = \frac{W \times L^3}{48 E_c I_c} = \frac{(2400 \times 9.8 \times 0.305 \times 0.56 \times 4.107) \times (4.107)^2}{48 \times (24100 \times 10^6) \times (0.305 \times 0.56^3/12)} = 0.2 \text{ mm} \tag{29}$$

It is observed that the values calculated above (totally 69.2 mm) are similar to the results obtained from VecTor2 (67.9 mm), shown in Fig. 12 (load type 1) below. The difference is partially due to $\alpha_s < \alpha_c$, causing some internal restraint.

For the deflection-time curve under transient fire load, the three-key-node linear model is selected and given in Fig. 13 (load type 2). Compared to the thermal gradient imposed, the deflection-time curve presents a similar overall trend. Note that there is a lag in time, between the turning points in plots of the imposed thermal gradient (at 4 hours) and the deflection curve (at 5 hours). This lag is thought to be due to that the high thermal gradient after its turning point still contributes to the

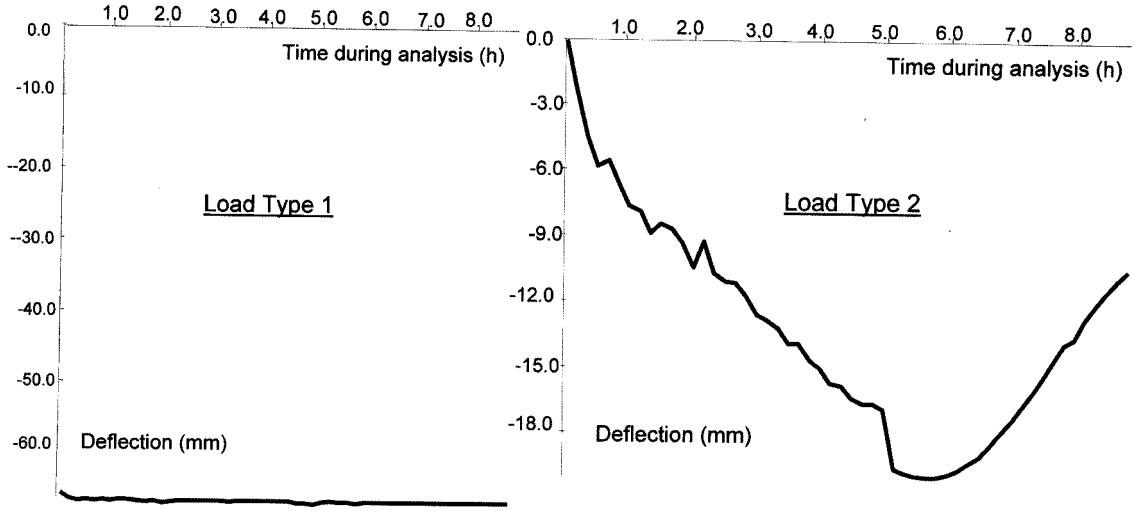

Fig. 13 Deflection-time curves in Problem 3

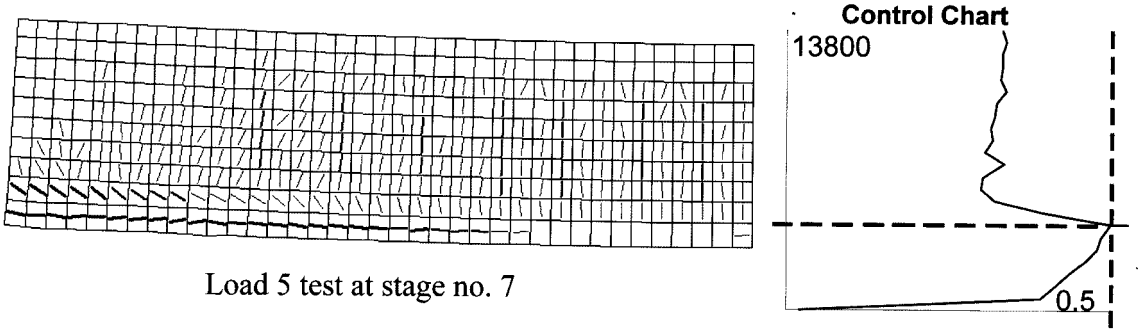

Fig. 14 Crack pattern in load 5 test in Problem 3

increase of the deflection until a lower stage is reached. This phenomenon is understandable if one considers the case where the imposed transient temperature load is constant but the resultant deflection is increasing as time proceeds.

• Stress and crack:

During the test of load types 4 and 5 (which are quite close to each other due to the similarity of the imposed thermal gradients), the structure failed at about 3.7 hours when the thermal load is extremely high (over 1100°C). In fact, the stiffness of the steel bars is completely lost in the bottom cracked concrete region due to high temperatures developed there (close to 1200°C), which produces a structural failure mechanism. The crack width (Fig. 14) at this moment is around 10 mm and the stress (Fig. 15) in the stirrups is well beyond the yield stress.

5.4. Problem 4: Thermal loaded portal frame

This problem is modeled after a specimen tested by Vecchio and Sato (1990). The specimen is, overall, a reinforced concrete portal frame consisting of two columns and one beam. Two side panels span the interior of the frame to form a tank-like structure, with a flexible silicone water-stop

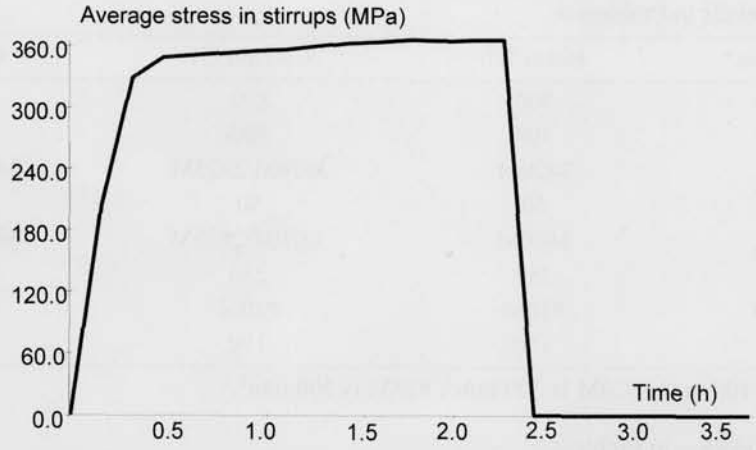

Fig. 15 Average stress in stirrups in load 4 test in Problem 3

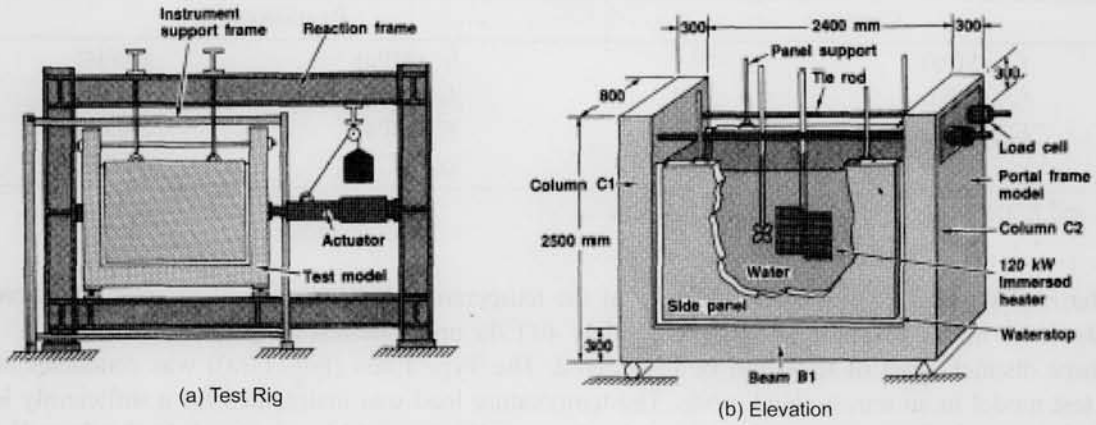

Fig. 15 Average stress in stirrups in load 4 test in Problem 3

in the gaps between the panels and the frame allowing the frame to be structurally independent of the panels. The schematic representation of the test model is shown in Fig. 16, with specimen details and material properties given in Table 4 and 5, respectively. By means of an immersed

Table 4 Specimen details in Problem 4

Specimen details*	Beam B1	Column C1	Column C2
b (mm)	800	800	800
h (mm)	300	300	300
A_s' (–)	3#20M	3#20M/2#25M	3#20M/2#25M
d' (mm)	50	50	50
A_s (–)	3#20M	3#20M/2#25M	3#20M/2#25M
d (mm)	250	250	250
A_v (–)	#10M	#10M	#10M
s (mm)	150	150	150

*: Area of #10M is 100 mm^2; #20M is 300 mm^2; #25M is 500 mm^2.

Table 5 Material properties in Problem 4

Material properties			
Concrete		Reinforcement*	
f_c' (MPa)	30.1	f_y (MPa)	450/445
f_{cr} (MPa)	3.10	f_u (MPa)	710/720
E_c (MPa)	30,000	E_c (MPa)	200,000
α_c (/°C)	12.1×10^{-6}	α_s (/°C)	12.0×10^{-6}

*: f_y and f_u are given for both 20M and 25M bars.

heater, water placed in the tank, originally at the temperature 15°C, was used to apply the thermal loads which increased at a rate of approximately 40°C/hr up to the test temperature 95°C.

Three distinct types of tests will be considered. The Type I test (Fig. 17(a)) was conducted with the test model in an unrestrained mode. The temperature load was maintained for a sufficiently long period so that both transient and final steady-state conditions could be observed. In the Type II test (Fig. 17(b)), the tie-rod was engaged to render the structure one-degree statically indeterminate. Thus, with the columns restrained from outward deflection by the tie-rod, restraint forces were induced in the tie-rod and hence in the frame. The temperature load was applied for about 8 hours, sufficient for the internal cracking and external restraint forces to fully develop. In the Type III test (Fig. 17(c)), the model was in the unrestrained configuration while a simultaneously acting mechanical load was applied laterally to the column at a location 680 mm above the centerline of the beam. The temperature load was applied until the ultimate capacity of the structure was attained under the monotonically increasing mechanical load. The computational model is shown in Fig. 17 (d), in which only half of the structure is modeled due to symmetry.

The results obtained from analyses are discussed below, in terms of the test type.

• Type I test:

During Type I testing, highly nonlinear transient thermal gradients are produced within the members in the beginning. In time, they approach a steady-state condition, characterized by a fairly linear gradient through the depth of the section. The imposed thermal loads result in an upward deflection of the beam relative to its ends and outward deflections of the column relative to its base. The vertical deflection occurring at the mid-span of the beam and the lateral deflection at the top of the column are shown in Fig. 18 (a and b). Both of them are thought to match the trend of the

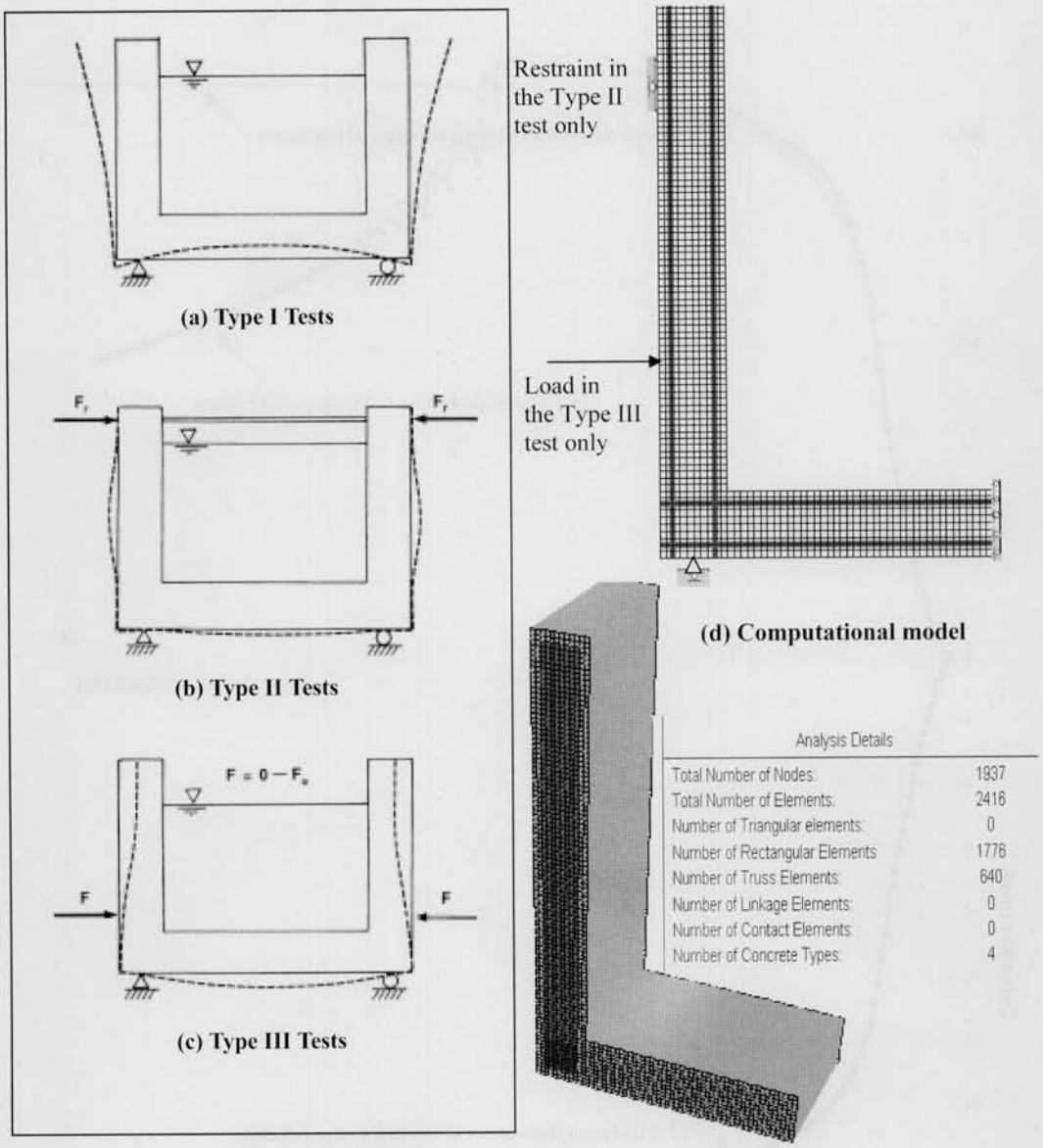

Fig. 17 Computational models in Problem 4

thermal load applied, increasing rapidly in the beginning and becoming constant in the end. During the time range of 12-24 hours, the deflection at beam's mid-span increases from 2.73 mm to 2.75 mm and the one at the column's top increases from 16.97 mm to 17.08 mm. That indicates the heat flow approaches the steady-state condition under which the deflection will theoretically stay unchanged.

Primary thermal stresses are induced in the test model, mainly due to nonlinearity in the thermal gradients shortly after the thermal loads are applied (also from differences in thermal expansion coefficients between concrete and reinforcement). However, these stresses diminish as the thermal

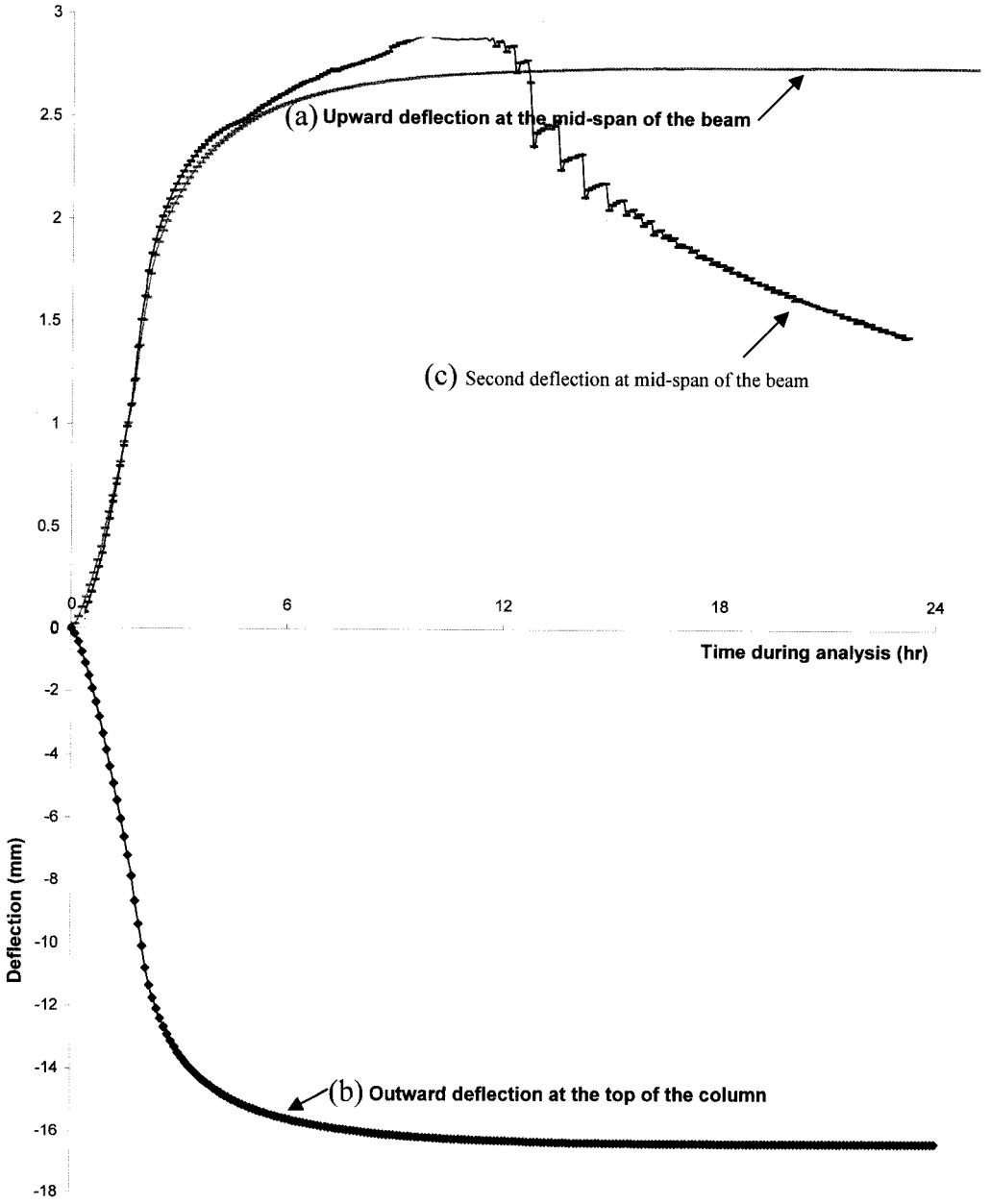

Fig. 18 Deflections in Type I test in Problem 4

gradients approach the linear steady-state condition. This expected phenomenon is well presented by Fig. 19, in which concrete's shear stress, within the element on the centerline of the column, approaches zero at conclusion of the test.

Compared to results from the laboratory work (Case PF3-B), the outward deflection of the column is quite close (17.1 mm vs 17.9 mm), while the upward deflection of the beam is quite different

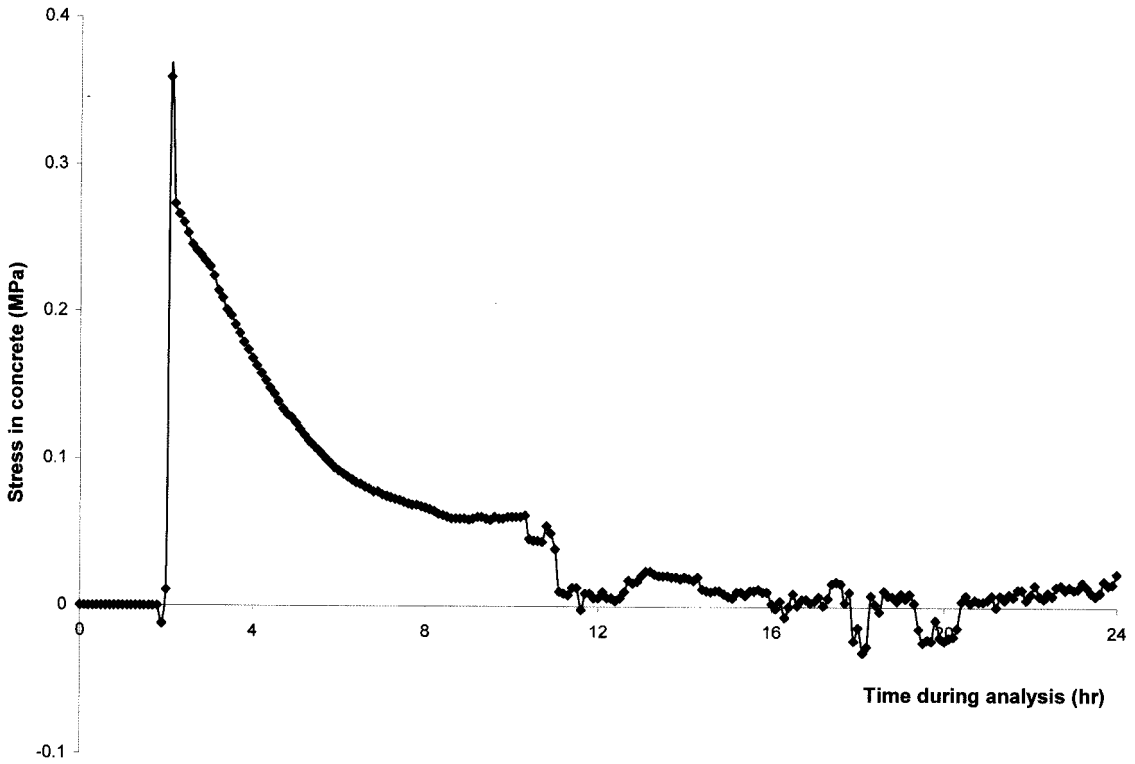

Fig. 19 Typical primary concrete stress in Type I test in Problem 4

(2.75 mm vs 1.65 mm). This overestimation is believed to be caused by the neglect of warming of the outside surface, which leads to a drop-off in thermal gradient applied. The computational results given above are, however, on the premise that temperature of outside surfaces remains unchanged. Without that assumption, one can expect that the conduction will never achieve the steady-state, as long as the water-supplied thermal load is present. A simulation under this circumstance is also conducted until 24hr, and the beam's corresponding deflections are given in Fig. 18(c). As seen, the beam's deflections are closer (1.50 mm vs 1.65 mm). This remaining underestimation is believed to be mainly caused by the so-called *skin effect*. This is because the exterior surface temperature is significantly higher than the surrounding air temperature. In practice, at conclusion of the test (24hr), the thermal gradient between two side-surfaces are going down to 55.1°C (59.6°C measured from laboratory work) from originally-imposed 78.4°C.

• Type II test:

In Type II testing, two tests are performed on the model. Case 1 represents the standard temperature load (80°C at 40°C/hr) with the 4.0 kN preload in the tie-rods, while there is no preload in tie-rods in Case 2. Shown in Fig. 20 are the restraint forces induced in the model under the above defined two conditions.

Generally, the time when the peak restraint forces occur do not correspond to the time of the peak thermal gradients. For instance, in Case 1, the restraint force peaks at 3.33 hr while thermal load attains the peak value at 2.0 hr. After peaking, the force decreases gradually. Some responses of the model at time of peak restraint force are compared in Table 6, between Case 1 in the present test

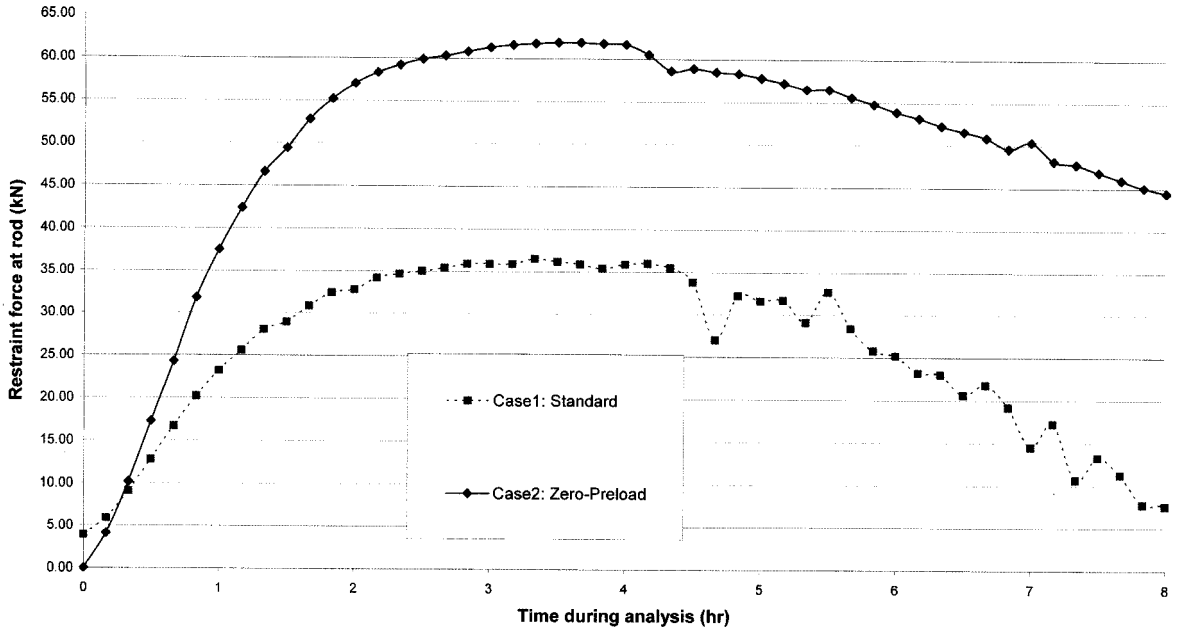

Fig. 20 Restraint force induced at engaged tie-rods in Type II test in Problem 4

Table 6 Comparison of results during Type II test

Test	F_r' (kN)	t (hr)	δ_b (mm)	δ_c (mm)	ε_{sbt} ($\mu\varepsilon$)	ε_{sbb} ($\mu\varepsilon$)	ε_{sct} ($\mu\varepsilon$)	ε_{scb} ($\mu\varepsilon$)
PF3-K	21.41	3.34	0.811	0.013	-356	701	-180	57
Case 1	36.30	3.33	1.306	0.007	-373	144	49	15

and Case PF3-K from the laboratory test. Part of the discrepancies is related to the fact that the test model was extensively cracked from previous testing. Here, it is modeled as initially uncracked. Also, playing a major part in the lower measured restraint forces is the influence of thermal creep. In addition, the analysis makes no attempt to model the complex physics relating to thermal skin effects, which result in a gradual increase in the outside surface temperatures and hence a decrease in the thermal gradient and restraint forces; rather, the boundary condition used in the modelling is based on the common assumption that the outside surface temperature remains equal to the ambient air temperature.

Similar to the case of thermal loading in a sense that the damage sustained shortly after the application of load will alter the member's long-term response, the cracking of concrete and/or yielding of reinforcement sustained by a structural member under previous loading will influence that member's response to newly applied loads (Vecchio 1987). To examine the effects of preload in the engaged tie-rods, Case 2 where there is no preload is tested. From Fig. 20, it is found that Case 2 develops much higher thermal-induced forces than does Case 1. Therefore, the preload in the tie-rods is seen to significantly influence the thermal-restraint forces induced. It is believed that thermal loads coupled with these mechanical loads expediate the cracking that renders the structure less stiff.

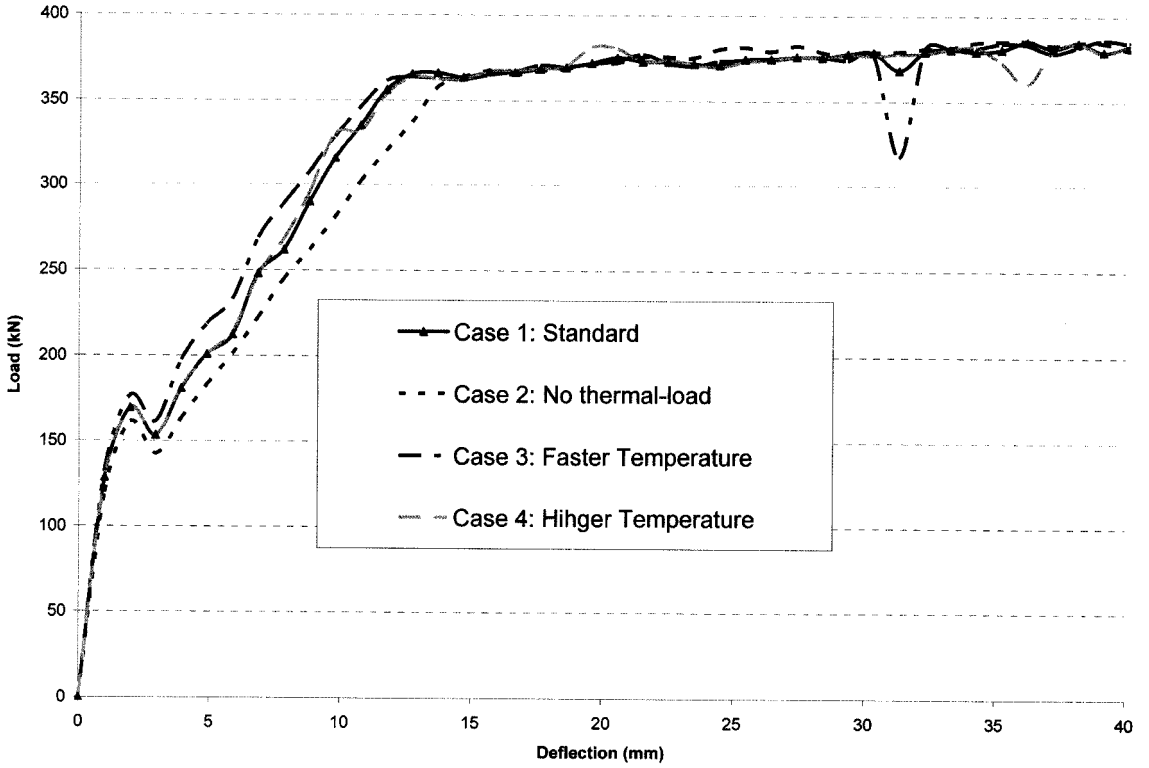

Fig. 21 Load-deformation curves in Type III test in Problem 4

• Type III test:

In this test, in addition to the temperature loading, a lateral applied load was monotonically increased until the ultimate capacity of the model was exceeded. A standard, faster, and higher temperature load are tested and specified as Case 1, 3, and 4 respectively. Case 2 then represents the test without temperature loads. As shown in Fig. 21, the load-deformation curves of the structure are linear in both un-cracked and cracked periods. The change of stiffness after cracking results in a less steep slope of the curve, which is clearly shown in Fig. 21. Thereafter, the bottom reinforcement in the beam yields, and in turn response becomes essential plastic with a limited increase in the load capacity, mainly due to strain hardening. The ultimate load capacity is approximately equal to predicted values obtained by using standard cracked-section analyses.

From comparisons, the presence of a thermal load in the case of test model does not appear to change the ultimate capacity of the structure very much. Notably, in this particular case, thermal loads are advantageous since they cause the deflection in the opposite direction to those caused by the applied mechanical load. However, if the thermal load is sufficiently high it can cause cracking of the structure when the mechanical load is still at a low level. In some cases, the presence of the thermal load may yield the structure much earlier than the case without thermal loads. A highly nonlinear thermal gradient will also induce primary stresses within the structure and reduce the stiffness and strength of the structure to a significant degree.

6. Conclusions

In this work, a 2D transient nonlinear thermal analysis capability is developed and implemented into a nonlinear finite element analysis procedure for reinforced concrete structures (program VecTor2). The nonlinear thermal analysis formulations are then coupled with a smeared rotating crack model for nonlinear mechanical analysis of cracked reinforced concrete structures. The smeared rotating crack approach, based on the Modified Compression Field Theory, provides a more accurate platform for analysis of concrete structures, particular those that are shear-critical, than that typically utilized by general purpose analysis programs (e.g. ANSYS). The implementation of nonlinear time-dependent thermal analysis capability with the domain of a smeared rotating crack model has not been previously reported and, hence, this work represents a new, and potentially improved, alternative to the analysis of concrete structures under transient thermal load conditions.

Acknowledgements

The authors wish to express their sincere gratitude for the discussion, suggestions and helps from Dr. Kruppa in Paris, Dr. Griffiths in Colorado, Dr. Lee in Singapore, and Dr. Bentz in Toronto.

Notation

$f(T)$ = Property modification factor at temperature T;
f_t = Concrete tensile strength;
f_c' = Concrete compressive strength;
ε_c' = Concrete strain corresponding to ε_c';
f_y = Yield strength of the reinforcing steel;
f_u = Ultimate strength of the reinforcing steel;
E_s = Modulus of elasticity of the reinforcing steel;
A_s = Cross-sectional area of bottom longitudinal reinforcement;
A_s' = Cross-sectional area of top longitudinal reinforcement;
A_v = Cross-sectional area of shear reinforcement;
b = Width of member cross section;
h = *Depth of member cross section;*
d = *Position of bottom longitudinal reinforcement;*
d' = Position of top longitudinal reinforcement;
s = *Spacing of shear reinforcement;*
F_r' = Peak restraint force in tie-rods;
δ_b = Deflection of beam at mid-span (downward positive);
δ_c = Relative deflection of columns at tie-rods (outward positive);
ε_{sbt} = Strain in beam bottom reinforcing bar at mid-span;
ε_{sbb} = Strain in beam top reinforcing bar at mid-span;
ε_{sct} = Strain in column outside reinforcing bar at base;
ε_{scb} = Strain in column inside reinforcing bar at base.

References

Belytschko, T. and Hughes, T. J. R. (1983), *Computational Methods for Transient Analysis*, North-Holland, Amsterdam.

Castillo, C. and Durrani, A. J. (1990), "Effect of transient high temperature on high-strength concrete", *ACI Mater. J.*, **87**(1), 47-53.

Heinrich, J. C. and Pepper, D.W. (1999), *Intermediate Finite Element Method: Fluid Flow and Heat Transfer Applications*, Taylor & Francis.

Lewis, R. W., Morgan, K., Thomas, H. R., and Seetharamu, K. N. (1996), *The Finite Element Method in Heat Transfer Analysis*, Wiley.

Lie, T. T. and Kodur, V. K. R. (1996), "Thermal and mechanical properties of steel-fiber-reinforced concrete at elevated temperatures", *Canadian. J. Civ. Eng.*, **23**(2), 511-517.

Ozisik, M. N. (1994), *Finite Difference in Heat Transfer*, CRC Press, USA.

Shin, K. Y., Kim, S. B., Kim, J. H., Chung, M., and Jung, P. S. (2002), "Thermo-physical properties and transient heat transfer of concrete at elevated temperatures", *Nucl. Eng. Des.*, **212**(2), 233-241.

Vecchio, F. J. and Collins, M. P. (1986), "The modified compression-field theory for reinforced concrete elements subjected to shear", *J. Concrete Inst.*, **83**(2), 219-231.

Vecchio, F. J. (1987), "Nonlinear analysis of reinforced concrete frames subjected to thermal and mechanical loads", *ACI Struct. J.*, **84**(6), 492-501.

Vecchio, F. J. (1990), "Reinforced concrete membrane element formulation", *ASCE J. Struct. Eng.*, **116**(3), 730-750.

Vecchio, F. J. and Sato, J. A. (1990), "Thermal gradient effects in reinforced concrete frame structures", *ACI Struct. J.*, **87**(3), 262-275.

Vecchio, F. J. (2000) "Disturbed stress field model for reinforced concrete: Formulation", *ASCE J. Struct. Eng.*, **126**(8), 1070-1077.

Zhou, C. E. and Vecchio, F. J. "Closed-form stiffness matrix for the four-node quadrilateral element with a fully-populated material stiffness", *ASCE J. Eng. Mech.*, **submitted**.

Zhu, X. K. and Chao, Y. J. (2002), "Effects of temperature-dependent material properties on welding simulation", *Comput. Struct.*, **80**(11), 967-976.

Zienkiewicz, O. C. and Taylor, R. L. (2000), *The Finite Element Method*, 5th edition, John Wiley & Sons.

CC